



# Parametric Analysis and Optimization of Inclined Laser Percussion Drilling of Carbon Fiber Reinforced Plastic Using Solid-State Nd: YAG Laser

Yadvendra Kumar Mishra<sup>1</sup> · Sanjay Mishra<sup>1</sup> · S. C. Jayswal<sup>1</sup>

Accepted: 29 July 2021 / Published online: 9 August 2021

© The Author(s), under exclusive licence to Springer Science+Business Media, LLC, part of Springer Nature 2021

## Abstract

Carbon fiber reinforced plastic (CFRP) is a next-generation material tailored for lightweight engineering applications. This study investigates the process of laser percussion inclined hole drilling (LPIHD) in CFRP, using an infrared laser of millisecond pulse duration. Parametric analysis to analyze the effect of input parameters like laser current (I), pulse width (Pw), gas pressure (Gp), workpiece thickness (Ti), and angle of incidence ( $\theta$ ) on geometrical hole characteristics, i.e., hole circularity at the top (HCT), hole circularity at the bottom (HCB) and hole taper (HT) has been carried out for LPIHD using Nd: YAG laser. A second-order regression model for each output response is developed using the Box-Behnken approach (BBD) of response surface methodology (RSM) and parametric analysis performed using RSM plots. Both the single objective optimization (SOO) and multiobjective optimization (MOO) of the LPIHD process were carried out using the desirability approach of RSM. The hole was analyzed using scanning electron microscopy (SEM) and energy dispersive X-ray (EDX). It has been observed that LPIHD at high current (300 A) and high pulse width (6 ms) produce a hole with HCT (0.68), HCB(0.65), and HT (6.5°). CFRP of small thickness gives high HCT (0.8), HCB (0.8), and low HT (4°) at high current (300 A). The MOO using the desirability approach, produce a hole of HCT (0.9297), HCB (0.9138), and HT (0.1784). The SEM images reveal that hole produced at input parameters corresponding to MOO has better surface integrity than the hole corresponding to SOO of HCT.

**Keywords** Inclined percussion drilling · CFRP · Circularity · Hole taper · RSM · Nd: YAG

---

✉ Sanjay Mishra  
smme@mmmut.ac.in

<sup>1</sup> Madan Mohan Malaviya University of Technology, Gorakhpur, Uttar Pradesh, India

## Introduction

A cavity in a solid workpiece having a depth-to-diameter ratio greater than 1:5 is called a hole. Based on its diameter, it is classified as a large hole ( $> 1$  mm) or a slight hole ( $> 1$  mm). [1]. It may be blind or through, and based on its orientation, we can also classify it as horizontal, vertical, or inclined. Mechanical drilling using a drill bit is the most widely used conventional drilling (CD) method. Various types of drill bits like split, crankshaft, and spiral points have further increased mechanical drilling application in modern industries [2]. Peck-drilling is used to produce large number of small holes in fragile components for electronic industries [3].

CFRP is a preferred material in those engineering applications which require lightweight materials with good mechanical properties. It is widely used in aviation, biomedical, and sports goods etc. Nowadays, CFRP is also used to fabricate the tail structure of the airplane, trailing-edge flaps, and spoilers in airplanes wings etc. Bending actuators and micro hinges of microrobots containing inclined holes made up of CFRP. Inclined micro holes in CFRP are used to attach fiber optic sensors for measuring temperature, thermal strain, and cracks, among other things. [4]. The property of high dimensional stability, low thermal expansion coefficient, with high biological and chemical inertness make CFRP a preferable material for missiles, aircraft brakes, and medical applications like prosthesis, surgery, x-ray equipment, radiological equipment, and pump components etc. [5].

In micro-components, the degree of integration between various components requires geometrically accurate holes with good surface integrity. The inherent heterogeneity and anisotropy, high heat sensitivity, and abrasivity of carbon fiber (CF) make CFRP a challenging material for machining. Since traditional engineering materials are being replaced with CFRP in most engineering applications, efficient machining of CFRP will help industries adopt CFRP more effectively in new applications. Poor hole quality nearly accounts for 60% of part rejection in modern manufacturing industries [6]. Since drilling is the last machining operation to be performed on any finished part; therefore, rejecting components due to poor hole quality must be avoided. The conventional methods of hole fabrication usually produce defects like micro-cracks at the inner surface of the hole, which deteriorates the fatigue life of the components [6]. Delamination and fiber pull-out is another major deterrent for CD of CFRP [7].

Furthermore, it is also difficult to produce small holes in inaccessible areas with CD. Therefore, the CD method cannot create high-density holes with close tolerance in CFRP [7, 8]. Speed, accuracy, repeatability, and ability to drill inclined holes make laser beam drilling (LBD) a preferable machining technique for creating high-density inclined holes in CFRP [9].

Depending on the relative orientation of the laser beam and drilling surface, LBD techniques can be static or dynamic. In static drilling, the removal of material occurs due to a series of pulses where the workpiece and laser beam are stable. Static drilling can further categorize as (i) pulse drilling: a single pulse accomplishes the drilling operation (ii) percussion drilling: a large number of consecutive laser pulses are used at a single point to remove the material from

the workpiece. The percussion laser drilling technique is static because both the workpiece and laser beam are at the same position during the entire drilling process and material removal from the workpiece due to repetitive laser interaction. Laser trepan drilling is dynamic drilling because to produce a hole in a workpiece, the laser beam first makes a central hole and then moves towards the circumference of hole to create hole [10].

In LBD, tapered holes are usually produced due to divergence of the laser beam after the focal position [11]. The contrasting thermal response of reinforcement and matrix in CFRP further deteriorate the hole geometry. Therefore, the creation of geometrically accurate holes with high circularity at the top and bottom (HCT, HCB) and low hole taper (HT) becomes very difficult during LBD [12]. The non-symmetrical nature of heat flow in the inclined hole, non-uniform melt ejection, and decline of laser power with depth are also responsible for poor hole geometry during LPHD [13].

Various investigations have been performed to analyze the effect of input process parameters on geometrical and other output characteristics during LBD of CFRP composites. Multiple authors have carried out experiments to study the effect of various laser and non-laser parameters on hole quality and its morphology during LBD of CFRP [9, 14]. The swelling behavior of three different carbon fibers, i.e., T-300, High Modulus (H.M.), and P100 during LBD of CFRP, were investigated by Voisey et al. [15]. French et al. [16] proposed that CO<sub>2</sub> as an assist gas reduces the thermal damage in CFRP during LBD. Anarghya et al. [17] observed that high energy density yields more circular craters and vice versa during LBD of CFRP. Salama et al. [18] adopted the multiple ring material removal technique to drill 6 mm thick CFRP using a 400 W picosecond (ps) laser.

Faas et al. [19] found that the ablation products eject at supersonic speed (3300 m/s) during LBD of 4.5 mm thick CFRP. Herzog et al. [20] concluded that Nd: YAG laser produces low HAZ and higher static and bending strengths in CFRP. It has been observed that a higher wavelength makes more HAZ during laser ablation of CFRP [21, 22]. Some authors have reported that ps pulsed laser produces low HAZ in CFRP during laser machining [23, 24]. Freitag et al. [24] proposed that heat accumulation can be reduced in CFRP by decreasing pulse overlaps with higher feed rates in an ultrafast laser system. Li et al. [25] introduced a multi-parallel ring technique to enhance the processing rate during single trepan drilling of CFRP.

Liu et al. [26] developed a finite element (FE) based model to predict the temperature and phase change during LBD of 2 mm thick CFRP. A Fourier method-based mathematical model to predict the geometry of drilled holes in PEEK composites reinforced with CF was proposed by Canel et al. [27]. Balasubramaniam et al. [28] compared the CD and LBD of 3 mm thick CFRP with 55% CF. Kumar and Singh [29] proposed addition of multi-walled carbon nanotubes to improve the quality of laser-drilled holes by reducing the decomposition temperature of Carbon and epoxy. Sobri et al. [30] concluded that in LBD of thick CFRP, spiral motion to the laser beam increases laser penetration. Tao et al. [31] proposed the opposite dislocation dual beam technique to drill 10 mm thick CFRP. Parametric analysis and multi-objective optimization (MOO) of laser percussion hole drilling (LPHD) in CFRP have been reported by several authors [32–38].

Shin and Mazumder [39] demonstrated the fabrication of inclined hole at  $30^\circ$  to the horizontal surface in Inconel 718 by helical laser drilling technique. LPHD at an angle of  $30\text{--}90^\circ$  were performed by Sezer et al. [40] on thermal barrier coated Nimonic 263 superalloy using Nd:YAG laser. It was reported that the recast layer and HAZ decrease with the increase of angle. Mullick et al. [41] investigated the effect of laser incidence angle on cut quality of stainless steel (4 mm) using Yb-fiber laser. Similarly, Schneider et al. [42] explored the effect of peak power and incidence angle during LPIHD using a long pulsed solid-state laser. The development of pressure and type of gas on hole quality were investigated by Okasha et al. [43] during LPHD of Inconel 718 at different drilling angles. The effect of angle of incidence on delamination during LPHD of thermal barrier coated Nimonic was studied by Kamalu et al. [44]. Leigh et al. [45] carried the statistical analysis for recast layer during LPIHD in nickel-based superalloy at  $30^\circ$  incidence angle. Angular holes ( $30^\circ$ ) using the laser trepan drilling technique in nickel superalloy were investigated by Matimuthu et al. [46]. Analysis of hole contours and ejection of plume at different inclination angle during LBD of graphite workpiece using Nd:YAG laser were done by Yao et al. [47]

The above literature survey reveals the following observations.

- a. Laser drilling of CFRP has been performed either by trepanning or helical drilling technique using short pulse (nanosecond) or ultrashort pulse (picosecond) laser. Furthermore, the majority of the work has been carried out either with fiber laser or  $\text{CO}_2$  laser.
- b. The majority of the laser drilling work in CFRP is associated with either laser trepanning or helical drilling techniques, with holes drilled at a right angle to the workpiece surface.
- c. Studies related to laser percussion drilling of CFRP are very few in number.
- d. Several studies have been performed on inclined laser drilling of superalloys or superalloys with thermal barrier coatings. But literature survey shows that a robust statistical model correlating different input process parameters with parameters related to geometrical accuracy of the hole, i.e., HCT, HCB, and HT, has not been reported for inclined laser drilling of CFRP.

Since the ms pulsed laser provides high peak power at an instant; therefore, the thermal load of this laser is low, and it also offers better productivity by reducing the processing time [48]. Currently, no literature is available for the LPIHD of CFRP. Therefore, in this study, statistical modeling and parametric analysis have been carried out to analyze the effect of input parameters on geometrical characteristics of HCT, HCB, and HT during LPIHD in CFRP of different thicknesses using ms pulsed Nd: YAG laser. To identify the "best" solution with the highest HCT, HCB, and lowest HT, single-objective optimization has been performed. Furthermore, the best-compromised solution based on the interaction among different conflicting objectives has also been achieved through MOO using the composite desirability approach of RSM. SEM and EDX analysis of the optimized hole has been performed to characterize the surface of the drilled hole.

## Materials and Methods

### Material

In this study, LPIHD performs on a CFRP of three different thicknesses at 0, 10, and 20° incidence angles. The CFRP was prepared by hand layup method with a fiber volume of 60%. The hand layup method is simple and well suited for low volume production because it does not require significant capital investment. The fiber volume fraction is responsible for the mechanical and physical properties of the CFRP. Here, 60% volume fraction has been taken because it gives good mechanical properties with strong interfacial adhesion between the carbon fiber and epoxy. Higher volume fraction (> 60%) may lead to poor wettability and infusion of the matrix into the carbon fibers [49]. The matrix of the composite was prepared by mixing Lapox L-12 epoxy resin with hardener K-6 at room temperature. Lapox L-12, medium viscosity epoxy resin, contribute to strength, durability, and chemical resistance to a composite. It possesses excellent shear strength, resulting in a strong interfacial bond with fibers resulting in good thermal stability and high degradation temperatures. Hardener K-6 maintains low viscosity, which gets cured at room temperature and mixes with epoxy resin to ensure a complete reaction. The required thickness of the CFRP was obtained using several layers of plain weave CF in an open mould. A roller was used to prevent an air trap from forming in the fiber. The prepared sample's thickness and flatness have been measured by the digital vernier caliper of the least count of 0.001 mm and a dial indicator.

### Experimental

The LPIHD experiments were performed on a fiber-optic delivered 250 W solid-state Nd: YAG operating at 1064 nm with 2–20 ms (ms) pulse duration. The machine is equipped with time shared fiber optic delivery system and kinematic mount and holder to tilt the laser beam in a controlled manner, as shown in Fig. 1a. A digital angle finder measured the angle by which the nozzle has been tilt. The maximum laser beam diameter was 400  $\mu\text{m}$ . Initially, pilot experiments were performed to select the feasible range of input parameters as shown in Table 1. Each experiment was repeated thrice, and the average of these repetitions were taken as the final value of output response. The actual experiments were performed using the box-Behnken design (BBD) approach of RSM. The output performance characteristics of HCT, HCB, and HT were determined by Eq. (1). The diameters mentioned in Eq. (1) were obtained using optical measuring microscope (Leica MC170 HD). Figure 1b illustrates the schematic of laser machining operation and cross-section of the drilled hole.

The process parameters have been selected so that the experimental model considers both the laser and non-laser parameters. Pulse current and pulse width are important to laser related parameters because the laser machine system used here is lamp-pumped solid-state Nd: YAG laser. The current control the peak power of

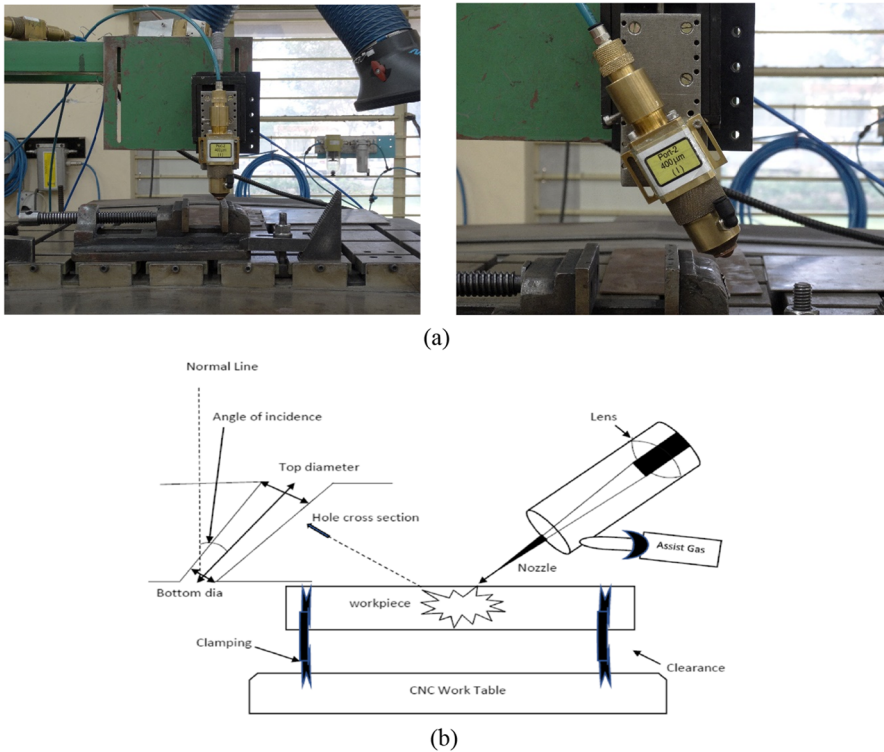


**Fig. 1** a Nozzle position during LPIHD, b schematic diagram of laser machining and hole cross-section

**Table 1** List of the actual and corresponding coded values for input parameter

Input parameters	Unit	Level 1	Level 2	Level 3	Level 3
Pulse Current ( $I$ )	ampere (A)	200	250		300
Pulse Width ( $P_w$ )	millisecond(ms)	2	4		6
Gas pressure ( $G_p$ )	Kg/cm <sup>2</sup>	4	6		8
Thickness ( $T_i$ )	Mm	1	3		5
Incidence angle ( $\theta$ )	degree (deg)	0	10		20

the system. The pulse width decides the energy of each pulse during laser material processing. Gas pressure was considered because it helps to reduce the thermal damage and helps to effectively remove the debris from the drill front during laser drilling. Since absorptivity of the laser beam by a material primarily depends on the thickness and angle of incidence, these two parameters were also incorporated for modeling.

The levels of input parameters were decided based on the pilot experiments so that a through hole is obtained during LPIHD. Pilot experiments were conducted

using one parameter at a time approach, i.e., varying one input parameter while the other remain constant. The angle of incidence was chosen based on machine capability, and the workpiece thickness was chosen based on a literature review.

Hole circularity is a dimensionless factor that measures the degree of proximity up to which a drilled hole resembles a perfectly circular shape. Ng and Li. [42] have defined average circularity as the ratio of the minimum to maximum hole diameter. Ghoreishi et al. [43] described the hole circularity as the ratio of maximum diameter ( $D_{max}$ ) to minimum diameter ( $D_{min}$ ) of the hole. In this study, the HCT, HCB, and HT have been determined using the Eq. 1.

The images of the actual drilled holes at different angle of incidence in the prepared samples has been shown in Fig. 2.

$$\left. \begin{aligned} HCT &= \left( \frac{D_{min}}{D_{max}} \right)_T \\ HCB &= \left( \frac{D_{min}}{D_{max}} \right)_B \\ HT &= \frac{D_T - D_B}{2 \times t} \end{aligned} \right\} \quad (1)$$

HCT, HCB, and HT determination require the evaluation of diameters, as shown in Eq. (1). These diameters can be obtained from the area of a circle. Therefore, after the drilling operation, The top and bottom surfaces of the drilled hole were polished with different grades of SiC paper, and then an ultrasonic cleaning system was used to remove small debris that had been inserted into the hole during polishing. For holes drilled at zero angles of incidence, the maximum and minimum diameters of the holes at the top and bottom surfaces were directly measured by image analysis software of optical microscope. But for holes drilled at another angle of incidence, an image corresponding to maximum and minimum area of both the entrance and exit side were obtained. These images were then projected at a vertical

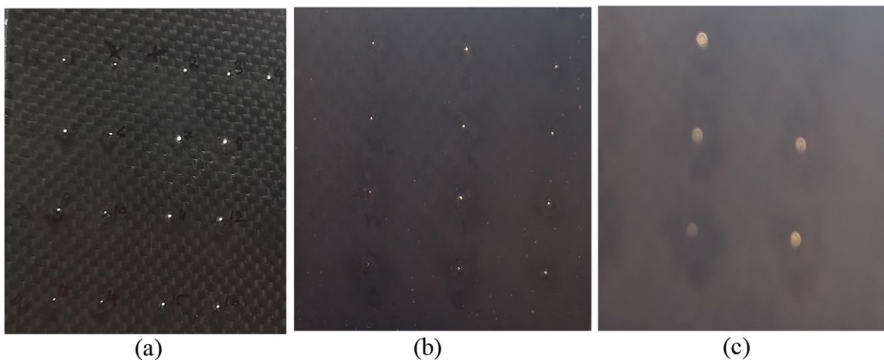


Fig. 2 LPIHD of CFRP a 1 mm at 0° b 3 mm at 10° c 5 mm at 20°



axis corresponding to zero angles of incidence using the image processing toolbox of MATLAB software.

The projected areas corresponding to maximum and minimum area were respectively used to determine the maximum ( $D_{max}$ ) and minimum diameter ( $D_{min}$ ) of the inclined holes. In order to reduce the probability of error due to variation in measurement, dimensions of each hole was measured thrice, and the average value of these three repetitions was finally used to determine the circularity and hole taper. The diameter at the top ( $D_{T}$ ) and bottom ( $D_{B}$ ) surfaces of the workpiece are the averages of  $D_{max}$  and  $D_{min}$  for the respective surfaces. The image of drilled holes at different angles is shown in Fig. 3. The images are at a different scale to avoid distortion of the image at higher magnification, particularly for inclined holes.

## Response Surface Methodology

RSM is used to develop a statistical model of machining processes that involve several input responses. It correlates the output performance characteristics of a machining process with input process parameters to simultaneously achieve a defined set of specifications for various outputs [35]. In this study, the BBD approach has been selected for developing the second-order regression model because it requires a smaller number of experiments, and it minimizes the chances of such a combination in which all the input factors are either at their highest or lowest level and thus avoid erroneous result due to extreme conditions. The BBD approach requires only three-level for each input to develop a second-order regression model. BBD is  $2^2$  full factorial design in which mid-level point between high and low level of the factors is used to maintain orthogonality. Therefore, only three-level of input parameters have been used here to conduct the experiments [48].

Unlike the central composite design (CCD) method of RSM, BBD is more convenient and time-saving because the model can be developed with fewer experiments for the same number of input factors [41]. Furthermore, it is also rotatable, ensuring that the developed model has the stable distribution of predicted variance within the experimental domain. The general second-order polynomial expression to analyze the parametric influences on the different output parameters is shown in Eq. 2.

$$y_u = \beta_0 + \sum_{i=1}^n \beta_i x_{iu} + \sum_{i=1}^n \beta_{ii} x_{iu}^2 + \sum_{i < j}^n \beta_{ij} x_{iu} x_{ju} \pm e_u \quad (2)$$

$\beta_0$  is a constant  $\beta_i, \beta_{ii}$  and  $\beta_{ij}$  are regression coefficients of linear, quadratic, and interaction terms, respectively.  $X_{iu}$  is the encoded values of the  $i_{th}$  machining parameters for the  $u_{th}$  experiment. The residual  $e_u$  is a measure of the experimental error of the  $u_{th}$  observations. The observed data from the set of experiments, as shown in Table 2 have been used as inputs to MINITAB software to establish mathematical models. Optimization to achieve the optimum value of HCT, HCB and HT has been carried out using the composite desirability approach of RSM.



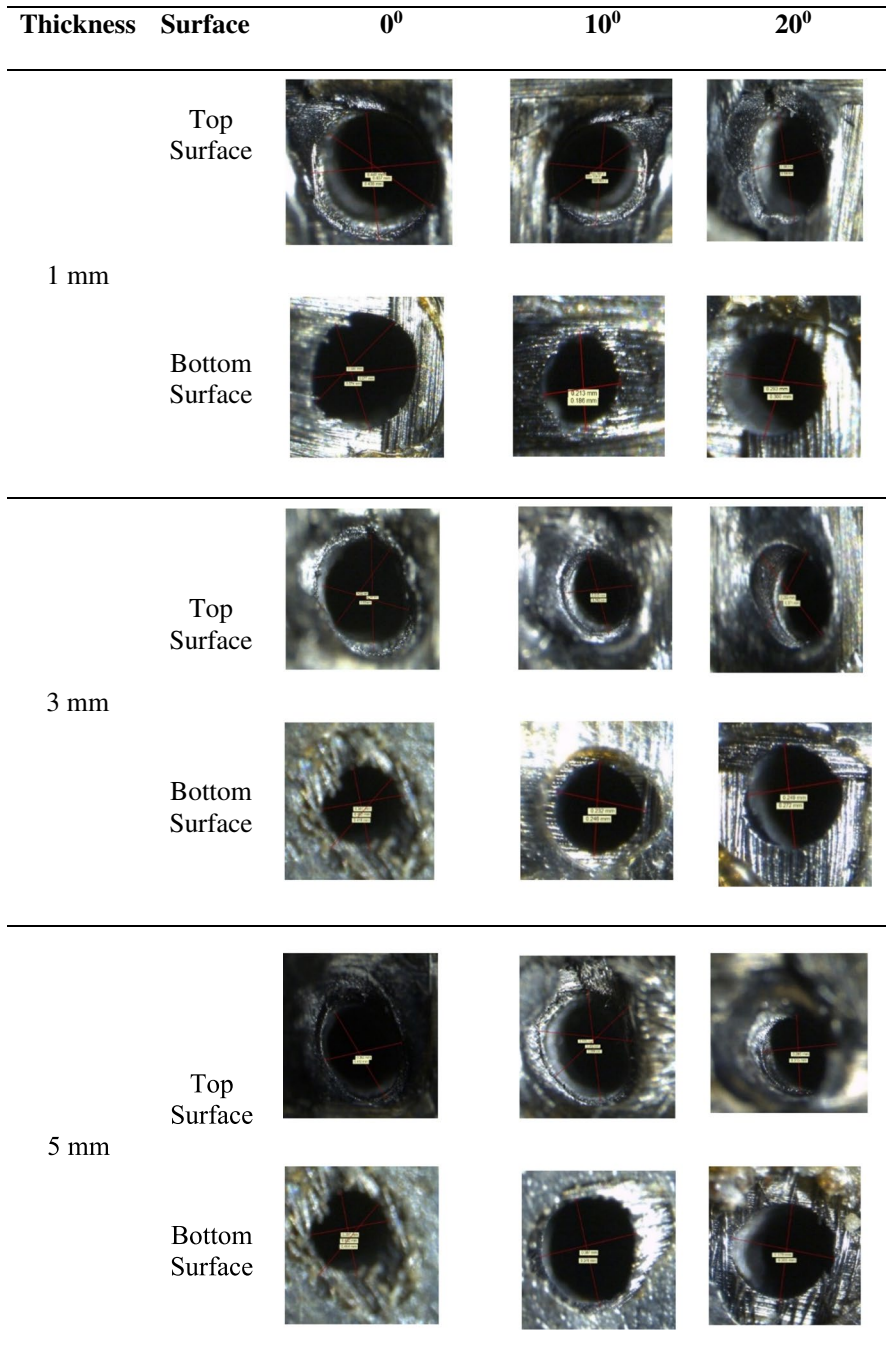


**Fig. 3** Microscopic image of LPIHD of CFRP of different thickness at different angles

**Table 2** Experimental plan showing values of process parameter and observed responses

Run order	Process Variable					Responses		
	current (A)	Pulse width (ms)	Air pressure (kg/Sq.cm)	Thick-ness (mm)	Angle of incidence (°)	HCT	HCB	Taper (°)
1	200	2	6	3	10	0.654	0.636	6.329
2	300	2	6	3	10	0.639	0.558	7.928
3	200	6	6	3	10	0.686	0.653	7.877
4	300	6	6	3	10	0.683	0.630	7.502
5	250	4	4	1	10	0.702	0.745	4.653
6	250	4	8	1	10	0.715	0.740	4.853
7	250	4	4	5	10	0.604	0.448	9.860
8	250	4	8	5	10	0.602	0.698	9.418
9	250	2	6	3	0	0.893	0.729	2.656
10	250	6	6	3	0	0.914	0.768	2.063
11	250	2	6	3	20	0.494	0.411	11.423
12	250	6	6	3	20	0.542	0.456	10.181
13	200	4	4	3	10	0.608	0.556	7.326
14	300	4	4	3	10	0.660	0.599	6.953
15	200	4	8	3	10	0.752	0.762	6.803
16	300	4	8	3	10	0.667	0.595	7.160
17	250	4	6	1	0	0.939	0.838	0.699
18	250	4	6	5	0	0.864	0.674	3.703
19	250	4	6	1	20	0.639	0.454	6.324
20	250	4	6	5	20	0.419	0.427	13.459
21	250	2	4	3	10	0.576	0.492	7.324
22	250	6	4	3	10	0.638	0.574	8.739
23	250	2	8	3	10	0.681	0.624	7.652
24	250	6	8	3	10	0.697	0.640	6.979
25	200	4	6	1	10	0.642	0.668	4.985
26	300	4	6	1	10	0.775	0.856	4.435
27	200	4	6	5	10	0.681	0.781	10.828
28	300	4	6	5	10	0.601	0.424	9.783
29	250	4	4	3	0	0.890	0.740	2.711
30	250	4	8	3	0	0.941	0.787	2.066
31	250	4	4	3	20	0.473	0.367	11.516
32	250	4	8	3	20	0.561	0.498	11.648
33	200	4	6	3	0	0.981	0.855	2.697
34	300	4	6	3	0	0.913	0.782	1.427
35	200	4	6	3	20	0.532	0.514	10.433
36	300	4	6	3	20	0.548	0.445	11.123
37	250	2	6	1	10	0.673	0.688	4.458
38	250	6	6	1	10	0.738	0.792	5.132
39	250	2	6	5	10	0.593	0.563	9.824

**Table 2** (continued)

Run order	Process Variable					Responses		
	current (A)	Pulse width (ms)	Air pressure (kg/Sq.cm)	Thick-ness (mm)	Angle of incidence (°)	HCT	HCB	Taper (°)
40	250	6	6	5	10	0.597	0.563	9.858
41	250	4	6	3	10	0.645	0.576	7.258
42	250	4	6	3	10	0.650	0.586	6.398
43	250	4	6	3	10	0.665	0.556	7.468
44	250	4	6	3	10	0.635	0.596	6.426
45	250	4	6	3	10	0.655	0.546	7.396
46	250	4	6	3	10	0.675	0.584	6.481

### Response Surface Model

The number of experiments (N) required for the development of BBD is defined as  $N=2k(k-1)+C_0$ , where  $k$  is the number of factors and  $C_0$  is the number of central points to be added to meet the iso-variance and orthogonality criteria [41, 50]. In this study,  $k=5$  and  $C_0=6$ ; therefore, the number of experiments shown in Table 2 is 46. Regression models as shown in Eqs. (3), (4), and (5) for HCT, HCB, and HT respectively has been developed based on these 46 experiments. While developing the regression models, the insignificant factors were not eliminated. When we eliminate a variable from a regression model, it indicates we are putting its regression coefficient equal to zero, even though the probable value for it as per the given data is different. This process moves us away from the prospective solution based on the actual theory, and we unintentionally get a suboptimal solution. Eliminating insignificant factors could also lead to unfavorable effects on the bias, i.e., the estimate of a given parameter may be either too high or too low [50].

$$\begin{aligned}
 \text{HCT} = & 0.440 - 0.00102I + 0.0398P_w + 0.1124G_p + 0.1445T_i - 0.04158\theta \\
 & + 0.000008I * I - 0.00166P_w * P_w - 0.00023G_p * G_p + 0.00013T_i * T_i \\
 & + 0.000639\theta * \theta + 0.000030I * P_w - 0.000343I * G_p - 0.000534I * T_i \\
 & + 0.000042I * \theta - 0.00283P_w * G_p - 0.00377P_w * T_i + 0.000339P_w * \theta \\
 & - 0.00091G_p * T_i + 0.000472G_p * \theta - 0.001812T_i * \theta
 \end{aligned} \tag{3}$$

**Table 3** S, R<sup>2</sup>, and R<sup>2</sup>(adj) value of responses

Responses	S value	R <sup>2</sup> value (%)	R <sup>2</sup> (adj) Value (%)
HCT	0.00945	95.57%	92.03%
HCB	0.01003	94.94%	90.90%
HT	0.00956	95.43%	91.78%

$$\begin{aligned}
 \mathbf{HCB} = & 0.939 - 0.00427I + 0.0075 P_w + 0.0736G_p + 0.1333T_i \\
 & - 0.02932\theta + 0.00002I * I + 0.00161P_w * P_w \\
 & + 0.00347 G_p * G_p + 0.01376T_i * T_i + 0.000038 \theta * \theta \\
 & + 0.000139I * P_w - 0.000525I * G_p - 0.001360I * T_i \\
 & + 0.000002I * \theta - 0.00411P_w * G_p - 0.00649 P_w * T_i \\
 & + 0.000075P_w * \theta + 0.01592 G_p * T_i + 0.001048 G_p * \theta \\
 & + 0.001705 T_i * \theta
 \end{aligned} \tag{4}$$

$$\begin{aligned}
 \mathbf{HT} = & 4.31 - 0.0312I + 0.525P_w - 0.999G_p + 1.401T_i + 0.125\theta \\
 & + 0.000065I * I + 0.0896P_w * P_w + 0.0841G_p * G_p + 0.0135T_i * T_i \\
 & - 0.00624\theta * \theta - 0.00494I * P_w + 0.00183I * G_p - 0.00124I * T_i \\
 & + 0.000981I * \theta - 0.1305P_w * G_p - 0.0401P_w * T_i - 0.0081P_w * \theta \\
 & - 0.0402G_p * T_i + 0.0097G_p * \theta + 0.0516T_i * \theta
 \end{aligned} \tag{5}$$

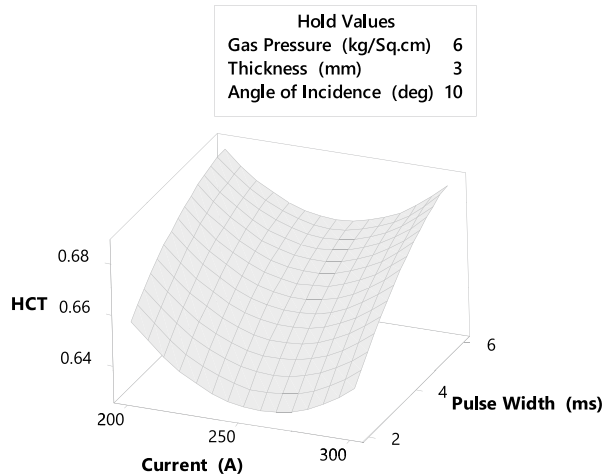
Table 3 shows a lower value of S for all the three output responses, which indicates that the obtained data are well fitted in the developed model and the experimental data are closer to the fitted line. R<sup>2</sup> is a statistical measure to know how close the data are to the fitted regression. R<sup>2</sup> value of unity indicates a better regression model. R<sup>2</sup> (adj) measures the proportion of variation explained by only those independent variables that help in defining the dependent variable. It prohibits us from adding an independent variable that does not help in predicting the dependent variable. Therefore, a higher value of R-sq and R-sq (adj), as shown in Table 3, indicates that all the obtained data are well fitted in the model developed for each response.

To check the adequacy of the developed models at 95% confidence level, analysis of variance (ANOVA) as shown in Table 4 has been implemented. The p-values for the sources like model, linear, and square terms are less than 0.05, indicating that model terms are significant, whereas only the interaction terms are a little higher than 0.05. The F-values represent the ratio of mean square due to a factor to the error of the mean square. The larger value of F indicates a higher effect of a factor on the response. It can be used to rank the order of various factors. Parameters with p-values smaller than the significance level are statistically significant.

**Table 4** ANOVA for HCT,HCB and HT

Source	HCT		HCB		HT	
	F-value	p-value	F-value	p-value	F-value	p-value
Model	27.00	0.00	25.83	0.00	26.12	0.00
Linear	79.15	0.00	74.64	0.00	77.07	0.00
Square	24.51	0.00	24.77	0.00	23.47	0.00
Interaction	2.16	0.057	1.95	0.086	1.97	0.082
Lack-of-fit	1.19	0.462	1.32	0.408	1.23	0.447

**Fig. 4** Surface plot for a combined effect of current and pulse width on HCT



The combined use of both F-value and p-value should be used while deciding about the suitability of the regression model. The combined analysis of the F-value and p-value helps ensure that the model's and its terms' F-values are not due to noise. If F-value is large, but the p-value is more than 0.05 (95% confidence level), it would indicate that a large F-value may be due to noise [51]. The details in Table 4 suggest that the developed models are adequate. Moreover, the higher p-values of lack of fit for all three output responses corroborate the fact that the developed model can predict the output response with good accuracy.

## Parametric Analysis of HCT, HCB and HT

In the subsequent section, the influence of input parameters on all the output responses, i.e., HCT, HCB, and HT, was explained using the response surface plots.

### Parametric Analysis of Hole Circularity at the Top (HCT)

Figure 5 shows the simultaneous effect of current and pulse width on HCT at  $G_p=6$  kg/sq.cm,  $T_i=3$  mm, and  $\theta=10^\circ$ . At a constant pulse width, the HCT decreases with the increase of current up to 250 A, and after that, it increases gradually till 300 A. It is also observed that HCT continuously increases with pulse width at constant current.

The increase of pulse width increases the pulse energy (pulse energy = Avg power  $\times$  pulse width) of the incident laser beam [52]. It also increases the thermal penetration depth ( $z=2\sqrt{(\alpha P_w)}$ , where  $z$  is thermal penetration depth,  $\alpha$  is the thermal diffusivity). Thermal conductivity of epoxy (0.245 W/mK) is very low compare to CF (50 W/mK) [23]. Therefore, heat gets quickly transferred to the epoxy, and thermal

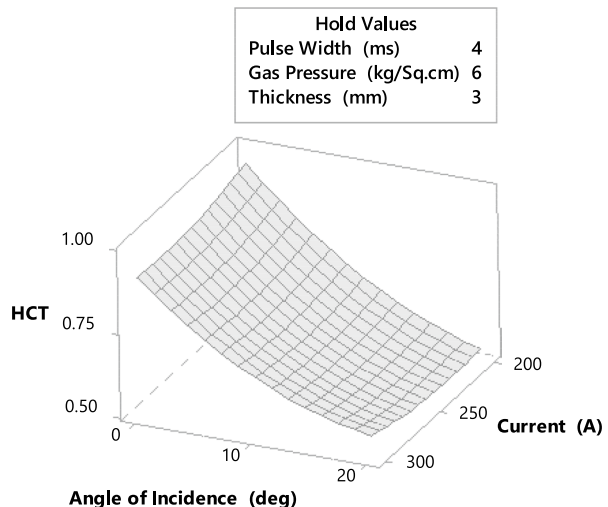
degradation of epoxy takes place. Due to the anisotropic nature of CF, thermal conductivity in the axial direction is very high, but in the traverse direction, the heat passes through the interface of fiber and epoxy. Therefore, the thermal conductivity of CFRP across the thickness is very low compared to in-plane conductivity [18].

The increase of thermal penetration depth creates a cavity in the CFRP, but due to poor thermal conductivity across the thickness, heat energy accumulation occurs. The matrix of the CFRP evaporates quickly due to its low vaporization temperature, but the CF remains attached to the surface [49]. Due to the poor thermal conductivity of CFRP across the thickness, a significant part of the energy obtained from the consecutive laser pulses were used to remove the attached CF, thereby increasing HCT.

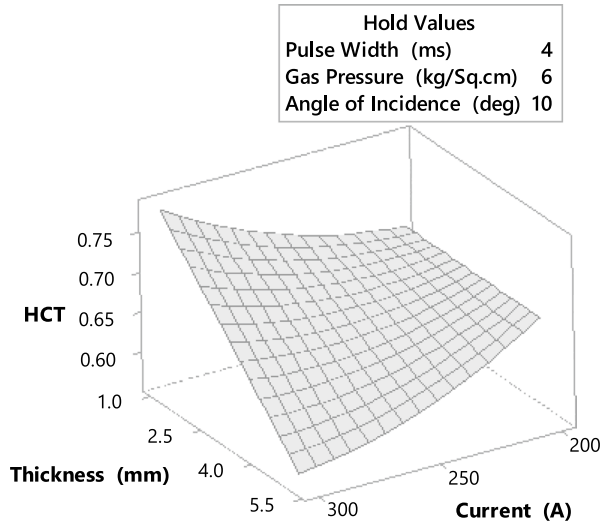
Figure 5 also shows that at  $P_w=2$  ms and  $I=200$  A, we get an HCT of 0.66, and as current increases, HCT decreases until 250 A, then gradually increases up to 300 A. When current is increased from 200 to 250 A at constant pulse width, laser energy increases at constant pulse width; therefore, peak power of laser beam increases and workpiece instantly receive very high energy. But due to constant pulse width, the thermal diffusion depth remains the same. Most of the heat is conducted away by the CF having high thermal conductivity in the axial direction [53]. As the laser irradiation time remains the same; therefore, a major part of thermal energy cannot ablate the CF but the epoxy gets ablated. Due to a slower heat transfer rate across the thickness, the energy available for CF ablation increases as the peak power increases owing to increase of current from 250 to 300 A [53].

Figure 4 demonstrates the combined effect of angle of incidence and current on HCT. It is observed that at a fixed current, the HCT decreases sharply with the angle of incidence. Furthermore, the increase of current at a certain angle of incidence gradually reduces the HCT. RSM plots also indicate that maximum HCT is obtained at  $\theta=0^\circ$  and  $I=200$  A due to the circular beam profile, producing high energy density. As the angle of incidence increases, the laser beam has to travel

**Fig. 5** Surface plot for the combined effect of current and angle of incidence on HCT



**Fig. 6** Surface plot for combined effect of current and thickness on HCT



a larger distance, and the beam profile becomes elliptical, which decreases the energy density and thus reducing the HCT [31]. Maximum variation of HCT with increase of current occurs at  $\theta=0^\circ$ . The growth of current increases the peak power, but since the pulse width remains fixed ( $P_w=4$  ms), the thermal penetration depth remains constant, and laser irradiation with high peak power will lead to rapid heating and, consequently, evaporation CF takes place [12]. As the current continues to increase, plasma formation occurs on the surface of the workpiece, which prohibits the further interaction of laser beam with the workpiece and thus reduces HCT [53].

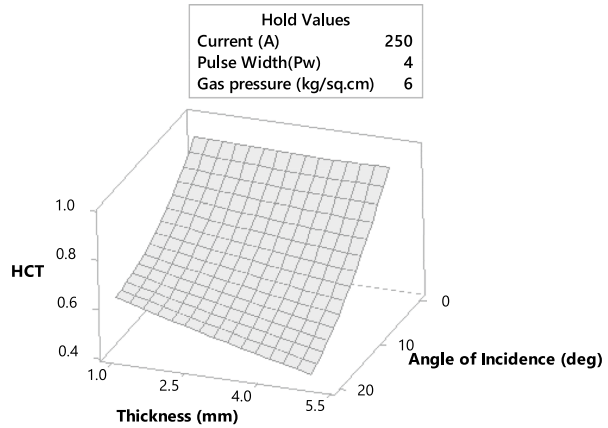
Figure 6 shows the simultaneous effect of thickness and current on HCT. It illustrates that combination of high current ( $I=300$  A) and low thickness ( $T_i=1$  mm) yields HCT value of more than 0.75. But, an increase in thickness at a high current ( $I=300$  A) significantly reduces the HCT. It is also observed from the response plot that change of thickness at a lower current ( $I=200$  A) do not have any major impact on HCT. Figure 6 also depicts that rise of current at a lower thickness ( $T_i=1$  mm) increases HCT, but as the thickness increase, nature of variation get change and at high thickness ( $T_i=5$  mm) a complete reverse trend has been observed.

At low current, the peak power density is low, and a large part of thermal energy is thermally conducted through CF. This would require a large number of laser pulses to create holes because the ablation of material largely depends on the optical energy absorbed by the workpiece. Due to good thermal conductivity along the CF, elliptical holes are usually obtained, giving low HCT. The increase of peak power at small thickness produces enough heat to vaporize both the CF and epoxy matrix. The assist gas will eject most of the vaporized particle and thus yielding high HCT.

The increase of workpiece thickness at high current ( $I=300$  A) necessitates many laser pulses to create a hole. The high peak power leads to the accumulation of large



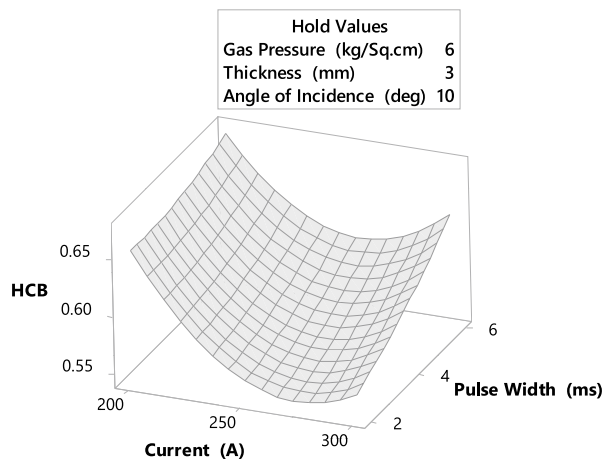
**Fig. 7** Surface plot for the combined effect of angle of incidence and thickness on HCT



thermal energy inside the workpiece, due to which plasma formation occurs. This phenomenon reduces the availability of thermal energy at the workpiece surface, resulting in the reduction of HCT. In contrast, when the thickness of the workpiece is varied at a small current ( $I=200$  A), the peak power is low and a large number of laser pulses are required to create the hole because the thermal penetration depth remains the same due to fixed pulse width. The thermal conductivity of CF across the thickness is relatively small compare to the axial direction; therefore, the accumulated heat combines with various heat spots within the hole to evaporate both the matrix and CF. The use of assist gas further improves the formation of the hole and thus, the HCT almost remain constant.

The combined effect angle of incidence and thickness on HCT is depicted in Fig. 7, which reveals the reduction of HCT with an increase of angle of incidence. At a low angle of incidence, the HCT increases very gradually with the thickness of workpiece, but at higher angle of incidence a gradual reduction has been observed

**Fig. 8** Surface plot for the combined effect of current and pulse width on HCB



at a higher angle of incidence. It can also be observed from Fig. 7 that angle of incidence has a more prominent effect on HCT.

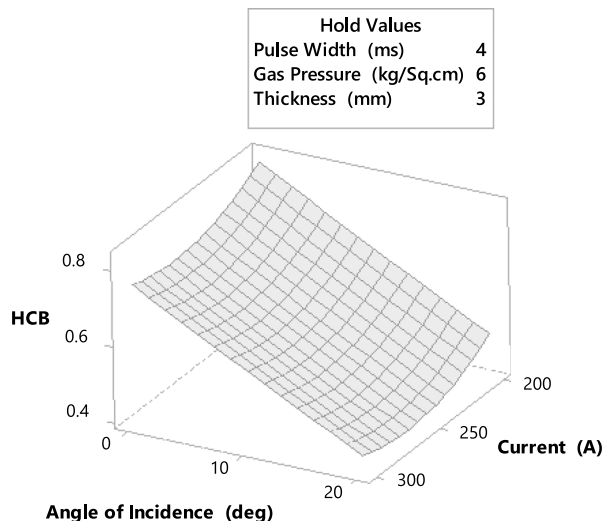
The energy density of laser beam decreases with the increase of angle of incidence, and subsequent change in beam profile from circular to elliptical also reduces the laser intensity [39]. Thermal conduction of heat in a preferential direction further deteriorates the HCT [30]. When the laser beam strikes the surface normally ( $\theta=0^\circ$ ) losses due to reflection are minimum. With the increase of hole depth, multiple reflections occur, and hot spot formation increases the laser beam's absorptivity [9]. When the thickness of the workpiece is low, laser pulses impart more heat in the radial direction at the top surface, thus increasing the HCT. When the laser beam strikes the workpiece at a certain angle of incidence, the intensity of transmitted light reduces because some part of the light is reflected back [54]. At high thickness, the direct interaction of laser beam with the inclined drilling front becomes complete, and challenging evaporation of CF does not take place, thus reducing the HCT.

### Parametric Analysis of Hole Circularity at the Bottom (HCB)

Figure 8 showed the behavior of HCB for current and pulse width when the LPHD performed at  $G_p=6$  kg/sq.cm,  $T_i=3$  mm and  $\theta=10^\circ$ . The increase of current at constant pulse width significantly decreases the HCB till 250 A, and after that, it begins to increase gradually till 300 A. When the current is constant, the HCB increases with pulse width, and the figure also depicts that at low current (200 A), the variation in HCB is within a narrow range. But as the current increases, the HCB increases significantly with pulse width.

The increase in current from 200 to 250 A increases the peak power of the laser, resulting in more laser energy being deposit in the laser spot. With the increase of depth, the beam's divergence reduces the laser energy density;

**Fig. 9** Surface plot for the combined effect of current and angle of incidence on HCB



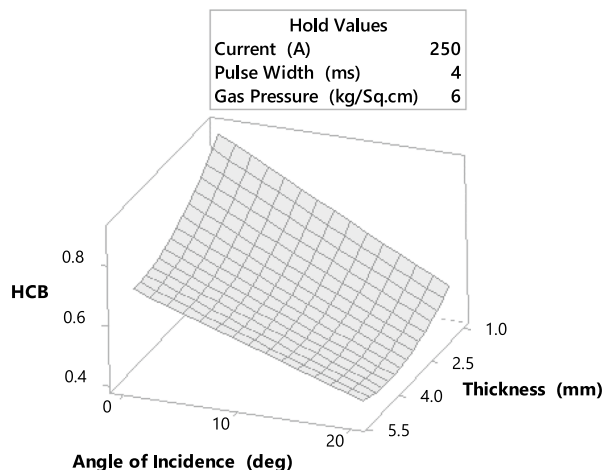
therefore, the thermal dissipation along the axial direction also decreases, which reduces the hole diameter [24]. Furthermore, thermal resistance at the matrix-CF interface minimizes the diameter of the hole across the thickness during LPIHD [55]. All these phenomena led to the increase in the number of laser pulses required to create a hole in CFRP. With the rise of current from 250 to 300 A, the energy density increases, and the CF evaporates directly, thus exposing the matrix to repeated laser beams. The direct sublimation of CF produces plasma, reflecting a part of the laser beam and prohibiting the effective interaction of the laser beam with the workpiece [12]. The assist gas helps break this plasma and allows the exchange of a high-energy beam with the workpiece, thus enhancing the HCB.

The increase of pulse width at high current (300 A) diffuses large thermal energy, quickly ablating the CF and epoxy matrix. As the pulse width increases, more and more thermal energy gets diffused from the center to the surrounding area, and at the same time, thermal penetration depth also increases. Therefore, HCB improves with the rise of the pulse width. When the pulse width increases at a low current (200 A), the thermal penetration depth rises, but heat diffusion to the surrounding area is insufficient to evaporate the CFRP or epoxy instantly. Due to the accumulation of heat, fiber swelling and mechanical erosion deteriorate the HCB [15].

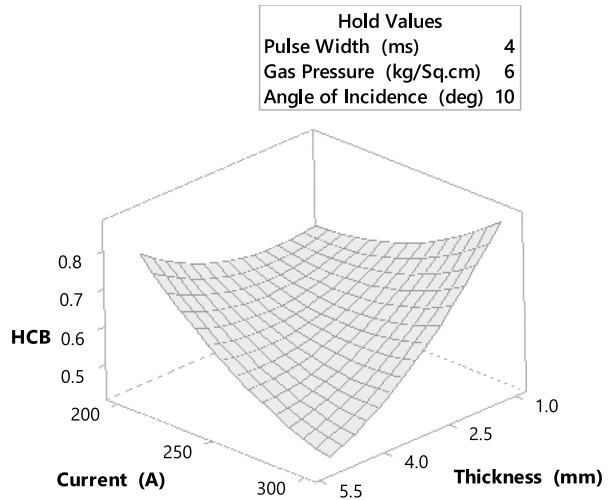
The RSM surface plots in Fig. 9 depict the effect of angle of incidence and current on HCB. It reveals that the HCB decreases with the angle of incidence. When the angle of incidence increases at constant current, the availability of peak power at certain depth decreases. Furthermore, increasing the angle of incidence makes a laser beam more elliptical, resulting in a reduction in laser beam intensity and, as a result, a decrease in HCB.

Figure 9 also reveals that an increase of current at a particular angle of incidence decreases the HCB. The increase of current increases the peak power, which increases the temperature faster, and direct sublimation of CF occurs, producing plasma. This plasma deviates the laser beam from the main path. The epoxy

**Fig. 10** Surface plot for the combined effect of thickness and angle of incidence on HCB



**Fig. 11** Surface plot for the combined effect of thickness and current on HCB

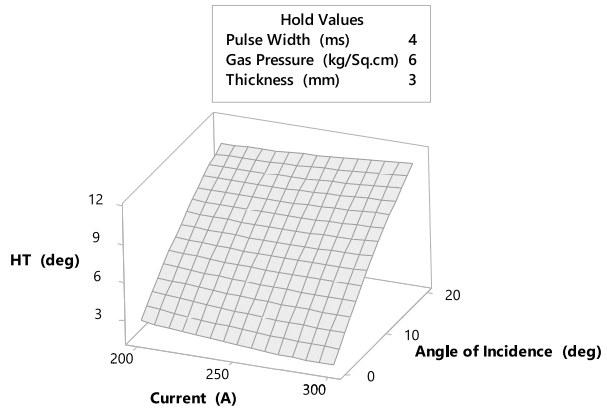


possessing a lower melting point melts and remains in molten condition for a long duration due to localization of the heat conducted away by CF [56]. With the increase of angle of incidence, the removal of material from the sidewall requires more laser energy. The combined effect of all these phenomena led to a reduction of HCB [47].

Figure 10 depicts that when the laser beam strikes the surface commonly ( $\theta=0^\circ$ ), the HCB decreases with thickness. The increase of angle of incidence reduces HCB. When the laser pulse hits the workpiece at constant current (250 A) and pulse width (4.0 ms), laser pulse energy remains constant. Initially, there is a quick transfer of heat in the axial direction; therefore, when the thickness is 1 mm, we get a hole with high HCB. However, as the workpiece thickness increases, the pulse energy decreases according to Lambert's Law. Phenomena of multiple reflections occur because the drilled hole wall absorbs some part of the energy, while others get scattered [54]. When the laser beam strikes the workpiece usually ( $\theta=0^\circ$ ), we get maximum energy density, and loss of laser intensity due to reflection and scattering is minimum. However, as the angle of incidence increases, the intensity of laser decreases and deviation occurs at the evaporation front of the drilled hole. [41]. The molten epoxy remains attached to the CF, and thus HCB reduces.

Figure 11 depicts the effect of thickness and current on HCB. Higher HCB is obtained either at low thickness (1 mm) and high current (300 A) or low current (200 A) at high thickness (5 mm). At higher currents (300 A), increasing the thickness reduces the HCB, but the opposite trend is observed (200 A). Similarly, an increase of current for a thick workpiece (5 mm) minimizes the HCB, but it shows an increasing trend at a small thickness (1 mm). As the experiments have been performed at  $\theta=10^\circ$ ; therefore, with the increase of thickness, the laser intensity reduces rapidly due to the laser beam's elliptical profile. The slant laser beam does not allow effective laser interaction with the erosion front. Therefore, the

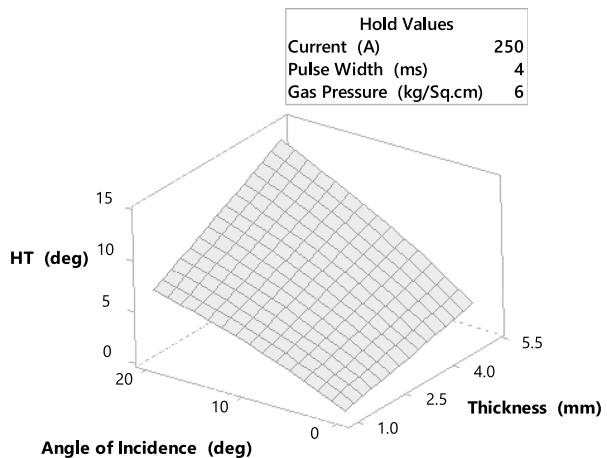
**Fig. 12** Surface plot for combined effect of angle of incidence and current on HT



evaporation rate of epoxy decreases which does not allow the formation of the circular hole at the exit side, thereby decreasing the HCB.

The enhancement of current increases the peak power of the laser, but for thick workpieces, the requirement of a large number of laser pulses to create a through hole led to the accumulation of thermal energy within the hole. As the depth increases, the accumulated thermal energy used to evaporate the matrix, due to which the CF remains attached to the wall of the drilled hole [56]. Assist gas reacts with the hot gasses inside the hole to enhance the temperature, but the thermal resistance at the matrix and CF further reduces the HCB. When the thickness is small, loss of power density due to contact resistance and depth is low; therefore, the laser beam combined with the assist gas create a clean hole at the bottom [55].

**Fig. 13** Surface plot for combined effect of angle of incidence and thickness on HT



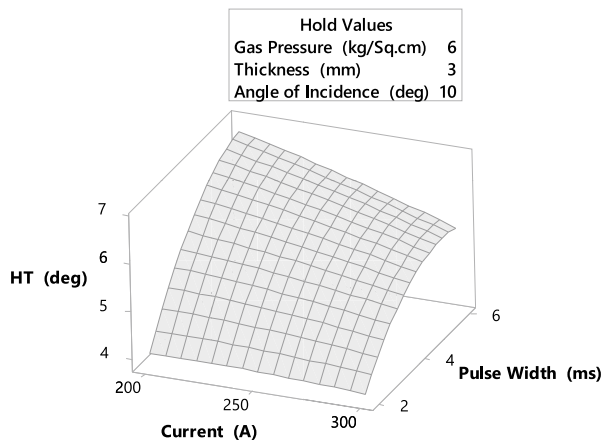
## Parametric Analysis of Hole Taper

Figure 12 illustrates that HT increases with the angle of incidence at constant current. When the angle of incidence is zero, the energy density is also high. Due to the large difference between the thermal properties of epoxy and CF, the epoxy decompose in the longitudinal direction of CF As per the Beer-Lambert law of absorption [52], a part of the energy given by laser beam remain present in the bulk material in the form of heat, because a fraction of pulse energy which is lower than the ablation threshold will heat the bulk materials [22]. Being an infrared laser, the Nd: YAG laser quickly pass through the matrix and directly heat the CF and resin scatter most of the laser power into the bulk material and produce high thermal load [12].

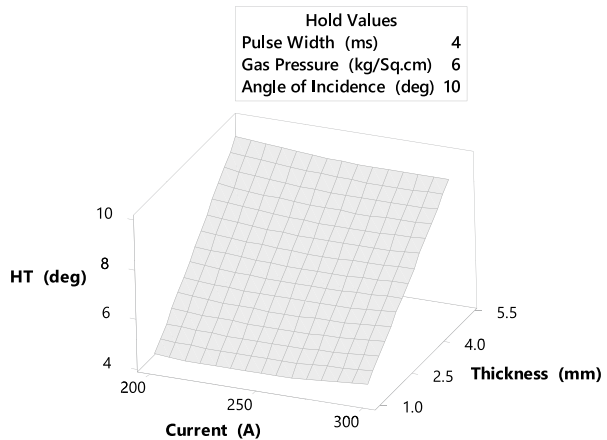
As the angle of incidence increases from  $0^\circ$ , the laser-irradiated area becomes elliptical in shape. Once the formation of the hole proceeds, the beam profile on the drilled front also begins to vary, and at a high angle of incidence, a large elongated beam profile would produce. As the depth of hole increases, the elongated beam profile delivers low energy density, which results in non-uniform heating of the drill front, and thus effective evaporation of CF and thermal decomposition of the matrix do not occur [56]. Furthermore, with the decrease of the laser intensity, the hole tends to become elliptical, and thus, HT increases. With the rise of current at a certain angle of incidence, heat transfer to CF increases rapidly; therefore, heating of the epoxy takes place, leading to its vaporization. But at the same time, the temperature of CF reduces, which stops the decomposition [53]. Therefore, the increase of current at a certain angle of incidence has only a marginal effect on HT.

When LPIHD is performed with a combination of low incidence angle and small workpiece thickness, a good quality hole with low HT is produced. As shown in Fig. 13, the HT increases with thickness, and its magnitude grows with increasing angle of incidence. When a laser pulse strikes the top surface of the workpiece commonly ( $\theta=0^\circ$ ), the top surface of the workpiece receives a very high energy till the existence of pulse, and CF get evaporates [34]. After the end of the pulse, the temperature gets stabilize at the evaporation temperature of epoxy.

**Fig. 14** Surface plot for combined effect of pulse width and current on HT



**Fig. 15** Surface plot for combined effect of thickness and current on HT

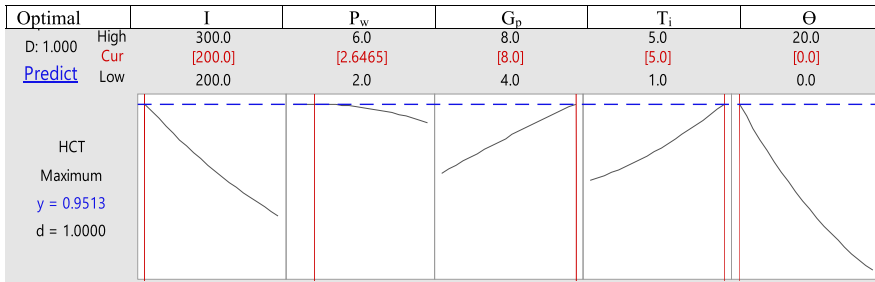


But with the progress of drilling operation across the thickness of the workpiece, the conduction of heat between two dissimilar materials with a huge difference between the thermal diffusivity and thermal conductivity takes place. Unlike at the top surface, where most of the heat propagation occurs along the CF only, the heat propagation occurs across the depth. The thermal conductivity of CFRP along the thickness is very low compared to in-plane [48]. The increase of thickness also increases the diffusion of heat in different directions, reducing the laser intensity, and therefore smaller hole is produced thereby increasing the HT.

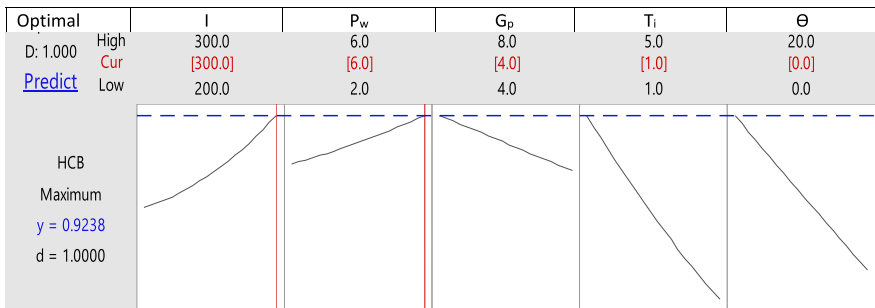
The analysis of the combined effect of current and pulse width on HT (Fig. 14) reveals that at lower current (200 A) and lower pulse width (2 ms), the taper is small. The increase of pulse width has a prominent effect on HT, and increase of current at high pulse width (6 ms) reduces the HT. At high pulse width, the thermal penetration depth is large, and as the current increases, more heat is infused into the workpiece. Therefore, HT decreases with the rise of current at high pulse width. The change of current at low pulse width (2 ms) has a marginal effect on HT because of low thermal diffusion depth and high contact resistance at the interface of the matrix and CF, the number of laser pulses required to create hole increases. When the matrix is heated, the CF surrounding the epoxy absorbs this heat and transfer it along the CF. This led to cooling of the epoxy matrix. Many laser pulses are required to create a hole. The slow accumulation of heat results in evaporation of the epoxy, and after that, the CF gets evaporated. Due to poor thermal conductivity across the thickness, the current change do not impart any significant deviation in the HT [48].

The RSM plots (Fig. 15) to analyze the combined effect of current and thickness on HT depict that the increase of current at a particular thickness does not have any significant effect on HT, but when thickness increases for a specific value of current, the HT increases significantly. The CF absorbs the IR laser pulses, and the epoxy gets heated during LPIHD. At the top surface, CF receives adequate heat for decomposition, and proper hole formation takes place. But when thickness increases at constant current, the amount of heat received by CF decreases, thereby reducing

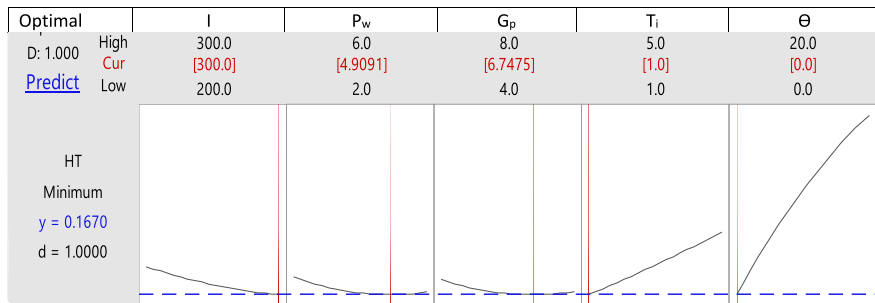




(a)



(b)



(c)

**Fig. 16** Single objective optimization of **a** HCT **b** HBT **c** HT**Table 5** Summary of Single objective optimization for HCT, HCB, and HT

Output parameters	Input process parameters				
	I	P <sub>w</sub>	G <sub>p</sub>	T <sub>i</sub>	θ
HCT	Low	Low	High	High	0°
HCB	High	High	Low	Low	0°
HT	High	High	High	Low	0°

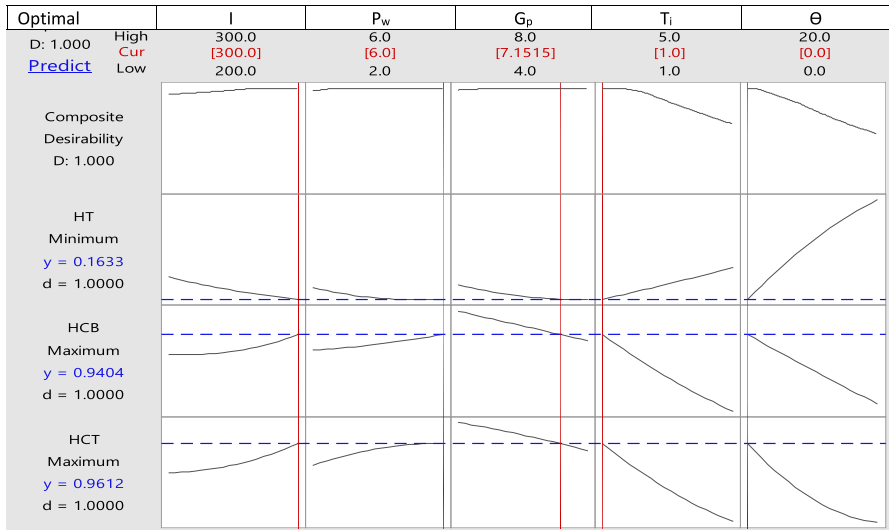


Fig. 17 Multiobjective optimization of HCT, HCB, and HT

heat transfer to the surrounding matrix. This phenomenon does not allow the formation of a clean hole with depth; therefore, the HT decreases [53].

### Single Objective and Multiobjective Optimization for LPHD of CFRP

#### Single Objective Optimization Of HCT, HCB, and HT

In single-objective optimization (SOO), the primary goal is to find the best combination of input process parameters, giving the minimum or maximum value of specific output responses depending on the nature of the problem. In this section, the SOO for LPIHD of CFRP performs using the desirability approach of RSM. Here, the effect of different input process parameters on the desirability of response has been evaluated. In the desirability approach, we convert the response to a desirability function in the range of zero to one. The desirability value becomes one when the output response achieves its target; otherwise, it becomes zero.

Table 6 Confirmatory experiments for single-objective optimization

Output parameters	Value obtained	Input process parameters					Experimental result	% error in prediction
		I	P <sub>w</sub>	G <sub>p</sub>	T	θ		
HCT	0.9513	200	2.6	8	5	0	0.9938	-4.25
HCB	0.9238	300	6.0	4.0	1	0	0.8921	3.43
HT	0.1670	300	4.9	6.7	1	0	0.1712	-2.51

**Table 7** Confirmatory experiments for multiobjective optimization

Output parameters	Value obtained	Input process parameters					Experimental result	% error in prediction
		I	P <sub>w</sub>	G <sub>p</sub>	T	θ		
HCT	0.9612	300	6	7.15	1	0	0.9297	3.27
HCB	0.9404						0.9138	2.82
HT	0.1633						0.1784	-9.24

Based on the above RSM prediction of SOO for HCT, HCB, and HT (Fig. 16a–c), we can summarize the findings as shown in Table. 5

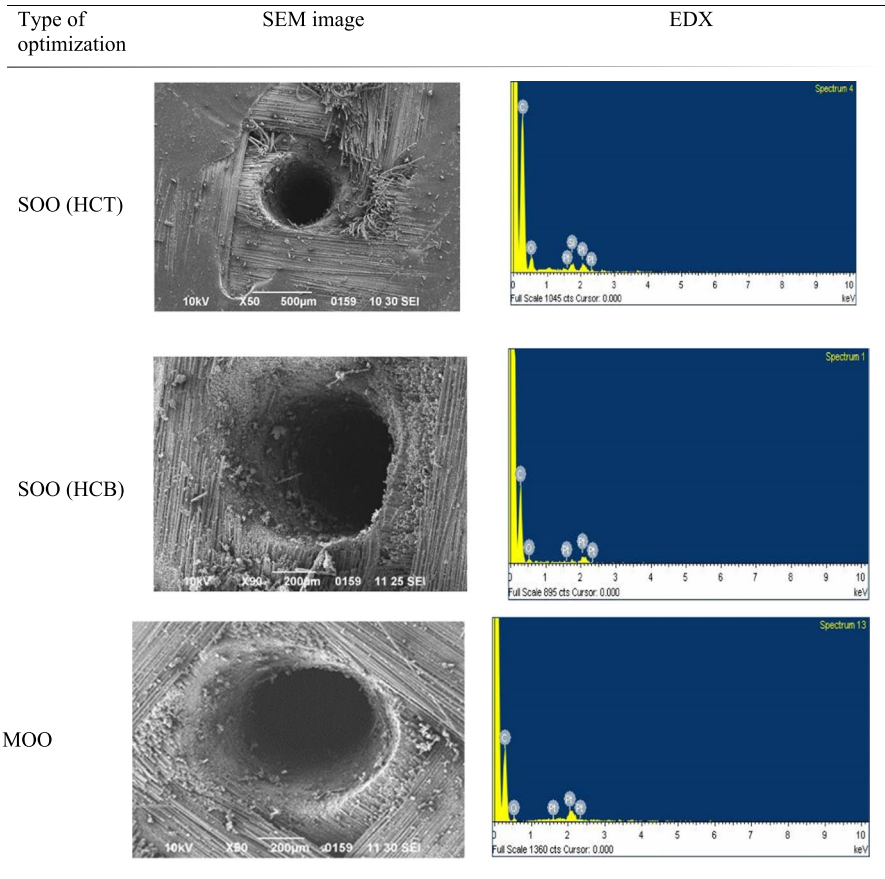
### Multiobjective Optimization of HCT, HCB, and HT

In MOO, we consider several conflicting objectives simultaneously. During LPHD, there is usually no single optimal solution, but a set of alternatives exists with different trade-offs. Therefore, the determination of a parametric combination which can simultaneously optimize multiple output characteristics is essential for LPIHD because the final output of the laser-drilled feature depends on the nonlinear interaction of selected input process parameters. Figure 17 shows the combination of input parameters that would produce a hole of minimum HT with high circularity at both surfaces.

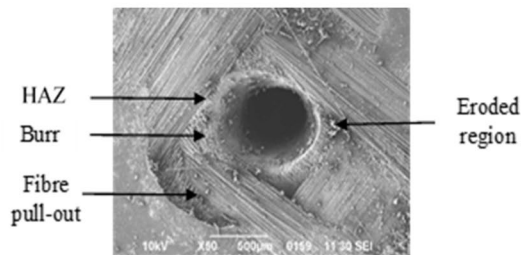
Figure 17 shows the graphical representation of MOO using the desirability approach of RSM. Each row of the graph represents an input variable, whereas the column indicates the output parameters considered during the LPIHD of CFRP. Each cell of the graph shows how the response variable changes as a function of one parameter, keeping other parameters constant. The vertical line inside the graph represents current parameter settings, and a horizontal dotted line represents the current response values. The numbers at the top of a column show the current parameter level settings. At the left side of each row, the goal for the output (maximum for HCT, HCB, and minimum for HT), predicted response (y) at current parameter settings, and individual desirability scores have been indicated. The current parameter settings are  $I=300$  A,  $P_w=6$  ms,  $G_p=7.15$  kg/cm<sup>2</sup>,  $T_1=1$  mm,  $\theta=0^\circ$  to achieve the maximum HCT and HCB of 0.9612 and 0.9404 respectively with minimum HT (0.1633 rad). The composite desirability factor (D) is shown in the upper left corner of the graph, and the value of the composite desirability factor is 1. Table 6–7 shows the details of confirmatory experiments to validate the improvement in output responses for the combination of input process parameters predicted by respective optimization techniques.

### SEM and EDX Analysis

SEM and EDX image of hole corresponding to SOO of HCT and HCB, MOO during LPIHD of CFRP is shown in Fig. 18a. Figure 18a depicts that the hole drilled at



(a)



(b)

**Fig. 18** a SEM and EDX image of the hole for SOO and MOO b defects in the laser drilled hole

the input parameter corresponding to SOO for HCT and HCB has extensive surface distortion even though a circular hole has been obtained. The SEM images show the presence of fiber debonding, matrix recession, and fiber pull-out on the top surface of the workpiece. But the hole drilled at parameters corresponding to MOO has more cleaner surface with less fiber breakage and pull out. The quantitative analysis

elemental composition of the laser drilled hole has been done with EDX as shown in Fig. 18a.

## Conclusions

IR Nd: YAG lasers of millisecond pulse duration has been used successfully to produce small diameter ( $< 1$  mm) inclined holes at three different incidence angles ( $0^\circ$ ,  $10^\circ$ , and  $20^\circ$ ) in CFRPs of thicknesses of 1 mm, 3 mm, and 5 mm. Second-order regression models were developed for output responses of HCT, HCB, and HT using the BBD approach of RSM. Parametric analyses were completed using the response surface plots to investigate the simultaneous effect of two input parameters on each output response during LPIHD. Both single objective and multiobjective optimization were carried out using the desirability approach of RSM. Based on the findings of this research, the following conclusions can be drawn:

- a) I.R. solid state Nd:YAG laser of ms pulse duration can be used to create small diameter ( $< 1$  mm) inclined holes in anisotropic and heterogeneous CFRP of thickness 1 mm, 3 mm and 5 mm.
- b) During LPIHD of CFRP, combination of high current (300 A) and high pulse width (6 ms) yields HCT (0.68), HCB (0.65) and HT ( $6.5^\circ$ ) at  $G_p = 6 \text{ kg/cm}^2$ ,  $T_i = 3 \text{ mm}$ ,  $\theta = 10^\circ$ . A change of pulse width from 2 to 6 ms, increases the HCT by 3% at 200 A. Furthermore, when the current increases to 300 A, the corresponding rise in HCT and HCB are 6.25% and 18%, respectively.
- c) HCT reduces by 20% when thickness increases from 1 to 5 mm at high current (300 A), whereas at low current (200 A), it increases by approx. 8% during LPIHD at  $P_w = 4 \text{ ms}$ ,  $G_p = 6 \text{ kg/cm}^2$ ,  $\theta = 10^\circ$ . Similarly, an increase of current from 200 to 300 A at 1 mm thickness increases the HCT by approx. 10%, but at 5 mm workpiece thickness, HCT decreases by 20%.
- d) During LPIHD, a combination of a high thickness (5 mm) and low current (200 A) produces high HCB (0.80) at  $P_w = 4 \text{ ms}$ ,  $G_p = 6 \text{ kg/cm}^2$ ,  $\theta = 10^\circ$ . Similarly, CFRP of small thickness (1 mm) yields high HCT (0.8), high HCB (0.8) and low HT ( $4^\circ$ ) at high current (300 A). At 200 A, increasing the thickness from 1 to 5 mm increases the HCB by 33%, but at high current (300 A), the HCB decreases by 37.5%. HT do not show any major deviation with the change of current at different thickness.
- e) Combination of high thickness (5 mm) and high angle of incidence ( $20^\circ$ ) at  $I = 250 \text{ A}$ ,  $P_w = 4 \text{ ms}$  and  $G_p = 6 \text{ kg/cm}^2$ , produce hole of high HT ( $15^\circ$ ) during LPIHD. At this angle, reducing the thickness from 5 to 1 mm reduces the HT by 50% while increasing the HCT and HCB by 50% and 20%, respectively.
- f) The desirability approach of RSM can be effectively used for the optimization of output responses in LPIHD. The confirmatory experiment for HCT, HCB, and HT corresponding to SOO, yield the values of 0.9938, 0.8921, and 0.1712, respectively, whereas, in the case of MOO, the corresponding values are 0.9297, 0.9138, and 0.1784. The SEM micrograph corresponding to SOO for HCT indicates a

circular hole with a large fiber break, high matrix recession, and fiber pull-out. But input parameters corresponding to the MOO of LPIHD produce circular holes with good surface integrity.

**Acknowledgements** The authors would like to express their gratitude to Dr. B.N. Upadhyaya, Raja Ramanna Centre for Advanced Technology (RRCAT) Indore, India for providing the experimental facility for this research work. India, for providing the Nd: YAG laser machining system to conduct the experiments for this study.

**Authors' Contributions** No.

**Funding** No funding received from any source.

**Availability of Data and Material (Data Transparency)** NoCode Availability (Software Application or Custom Code) Not applicable.

**Declarations**

**Conflict of interest** No conflict of interest.

## References

1. Raj, R.C.B., Ronald, B.A., Velayudham, A., Nayak, P.K.: Hole accuracy during deep hole drilling for hydraulic cylinder application. *Adv. Mater. Res.* **984–985**, 67–72 (2014). <https://doi.org/10.4028/www.scientific.net/AMR.984-985.67>
2. Ho Cheng, H., Tsao, C.C.: Effects of special drill bits on drilling induced delamination of composite materials. *Int. J. Mach. Tools Manuf.* **46**, 1403–1416 (2006)
3. Kim, D.W., Lee, Y.S., Park, M.S., Chu, C.N.: Tool life improvement by peck drilling and thrust force monitoring during deep-micro-hole drilling of steel. *Int. J. Mach. Tools Manuf.* **49**, 246–255 (2009)
4. Kumar, R., Kumar, A., Singh, I.: Electric discharge drilling of micro holes in CFRP laminates. *J. Mater. Process. Technol.* **259**, 150–158 (2018)
5. Pradere, C., Batsale, J.C., Goyhe'ne'che, J.M., Pailler, R., Dilhaire, S.: Thermal properties of carbon fibers at very high temperature. *Carbon* **47**, 737–743 (2009)
6. Liu, D., Tang, Y., Cong, W.L.: A review of mechanical drilling for composite laminates. *Compos. Struct.* **94**, 1265–1279 (2012)
7. Krishnaraj, V., Prabukarthi, A., Ramanathan, A., Elanghovan, N., Kumar, M.S., Zitoune, R., Davim, J.P.: Optimization of machining parameters at high-speed drilling of carbon fiber reinforced plastics (CFRP) laminates. *Compos.: Part B* **43**, 1791–1799 (2012)
8. Abel, A., Heilmann, M.: Deep hole drilling using tools with small diameters-process analysis and process design. *CIRP Ann. Manuf. Technol.* **61**, 111–114 (2012)
9. Rodden, W.S.O., Kudesia, S.S., Hand, D.P., Jones, J.D.C.: A comprehensive study of the long pulse Nd:YAG laser drilling of multi-layer carbon fibre composites. *Opt. Commun.* **210**, 319–328 (2002)
10. Fenoughty, K.A., Jawaid, A., Pashby, I.R.: Machining of advanced engineering materials using traditional and laser techniques. *J. Mater. Process. Technol.* **42**, 391–400 (1994)
11. Li, L., Low, D.K.Y., Ghosh, M.: Hole taper characterisation and control in laser percussion drilling. *CIRP Ann. Manuf. Technol.* **51**(1), 153–156 (2002)
12. Takahashi, K., Tsukamoto, M., Masuno, S., Sato, Y.: Heat conduction analysis of laser CFRP processing with I.R. and U.V. laser light. *Compos. Part A Appl. Sci. Manuf.* **84**, 114 (2016). <https://doi.org/10.1016/j.compositesa.2015.12.00>
13. Jain, V.K.: *Advanced Machining Processes*, pp. 3–5. Allied Publishers Private Limited, New Delhi (2008)

14. Masmiati, N., Philip, P.K., Mater, J.: Investigations on laser percussion drilling of some thermo-plastic polymers. *J. Mater. Process. Technol.* **185**, 198–203 (2007)
15. Voisey, K.T., Fouquet, S., Roy, D., Clyne, T.W.: Fibre swelling during laser drilling of carbon fibre composites. *Opt. Lasers Eng.* **44**, 1185–1197 (2006)
16. French, P.W., Wolynski, A., Naeem, M., Sharp, M.C.: New laser machine tools for processing carbon fibre reinforced plastic (CFRP). *Key Eng. Mater.* **496**, 30–35 (2011)
17. Anarghya, M., Nitish, S.R., Yatheesha, R.B., Gurumurthy, B.M., Ranjith, B.S.: Investigation of CO<sub>2</sub> laser drilled micro holes for heat affected zone and structural integrity in CFRP composites. *Int. J. Mater.* **3**, 33–43 (2016)
18. Salama, A., Yan, Y., Li, L., Mativenga, P., Whitehead, D., Sabli, A.: Understanding the self-limiting effect in picosecond laser single and multiple parallel pass drilling/machining of CFRP composite and mild steel. *Mater. & Des.* **107**, 461 (2016)
19. S. Faas, C. Freitag, S. Boley, P. Berger, R. Weber, T. Graf (2017) Flow speed of the ablation vapours generated during laser drilling of CFRP with a continuous-wave laser beam, *Appl. Phys. A Mater. Sci. Proces.* **123**,
20. Herzog, D., Jaeschke, P., Meier, O., Haferkamp, H.: Investigations on the thermal effect caused by laser cutting with respect to static strength of CFRP. *Int. J. Mach. Tools Manuf.* **48**, 1464 (2008)
21. Leone, C., Genna, S., Tagliaferri, V.: Fibre laser cutting of CFRP thin sheets by multi-passes scan technique. *Opt. Lasers Eng.* **53**, 43 (2014). <https://doi.org/10.1016/j.optlaseng.2013.07.027>
22. Dell'Erba, M., Galantucci, L.M., Miglietta, S.: An experimental study on laser drilling and cutting of composite materials for the aerospace industry using excimer and CO<sub>2</sub> sources. *Compos. Manuf.* (1992). [https://doi.org/10.1016/0956-7143\(92\)90178-W3](https://doi.org/10.1016/0956-7143(92)90178-W3)
23. Wolynski, A., Herrmann, T., Mucha, P., Haloui, H., L'huillier, J.: Laser ablation of CFRP using picosecond laser pulses at different wavelengths from U.V. to I.R. *Procedia Phys.* (2011). <https://doi.org/10.1016/j.phpro.2011.03.136>
24. Freitag, C., Onuseit, V., Weber, R., Graf, T.: High-speed observation of the heat flow in CFRP during laser processing. *Procedia Phys.* (2012). <https://doi.org/10.1016/j.phpro.2012.10.027>
25. Li, Z.L., Zheng, H.Y., Lim, G.C., Chu, P.L., Li, L.: Study on U.V. laser machining quality of carbon fibre reinforced. *Compos. Part A Appl. Sci. Manuf.* **41**, 1403 (2010). <https://doi.org/10.1016/j.compositesa.2010.05.017>
26. Liu, Y.C., Wu, C.W., Huang, Y.H., Song, H.W., Huang, C.G.: Interlaminar damage of carbon fibre reinforced polymer composite laminate under continuous wave laser irradiation. *Opt. Lasers Eng.* **88**, 91 (2017)
27. Canel, T., Bağlan, I.: Tamer Sımmazçelik, Mathematical modeling of heat distribution on carbon fiber Poly(etherether-ketone) (PEEK) composite during laser ablation. *Opt. Laser Technol.* **127**, 106190 (2020). <https://doi.org/10.1016/j.optlastec.2020.106190>
28. Balasubramaniam, V., Rajkumar, D., Ranjithkumar, P., Narayanan, C.S.: Comparative study of mechanical technologies over laser technology for drilling carbon fiber reinforced polymer materials. *Indian J. Eng. Mater. Sci.* **27**, 19–32 (2020)
29. Kumar, D., Singh, K.K.: Effect of nanofiller on fibre laser drilling quality of carbon fibre reinforced polymer composite laminates. *Proc. IMechE Part E: J. Process. Mech. Eng.* (2019). <https://doi.org/10.1177/0954408918812253>
30. Sobri, S.A., Heinemann, R., Whitehead, D.: development of laser drilling strategy for thick carbon fibre reinforced polymer composites (CFRP). *Polymer* **12**, 2674 (2020). <https://doi.org/10.3390/polym12112674>
31. Tao, N., Chen, Genyu, Tianyu, Yu., Li, W., Fan, L.: Dual-beam laser drilling process for thick carbon fiber reinforced plastic composites plates. *J. Mater. Process. Technol.* (2020). <https://doi.org/10.1016/j.jmatprotec.2020.116590>
32. Mathew, J., Goswami, G.L., Ramakrishnan, N., Naik, N.K.: Parametric studies on pulsed Nd:YAG laser cutting of carbon fibre reinforced plastic composites. *J. Mater. Process. Technol.* **89–90**, 198–203 (1999)
33. Negarestani, R., Li, L., Sezer, H.K., Whitehead, D., Methven, J.: Nano-second pulsed DPSS Nd:YAG laser cutting of CFRP composites with mixed reactive and inert gases. *J. Adv. Manuf. Technol. Int.* (2010). <https://doi.org/10.1007/s00170-009-2431-y>
34. Negarestani, R., Li, L.: Laser machining of fibre-reinforced polymeric composite materials. *Technol. Compos. Mater. Mach.* (2012). <https://doi.org/10.1533/9780857095145.2.288>



35. Vijayan, D., Rajmohan, T.: Modelling and evolutionary computation on drilling of carbon fiber-reinforced polymer nanocomposite: an integrated approach using RSM based PSO. *Soc. Mech. Sci. Eng. J. Braz.* (2019). <https://doi.org/10.1007/s40430-019-1892-7>
36. Biswas, R., Kuar, A.S., Mitra, S.: Multiobjective optimization of hole characteristics during pulsed Nd:YAG laser micro drilling of gamma-titanium aluminide alloy sheet. *Lasers Eng. Opt.* (2014). <https://doi.org/10.1016/j.optlaseng.2014.03.014>
37. Ng, G.K.L., Li, L.: The effect of laser peak power and pulse width on the hole geometry repeatability in laser percussion drilling. *Opt. Laser Technol.* **33**(6), 393–402 (2001)
38. Ghoreishi, M., Low, D.K.Y., Li, L.: Comparative statistical analysis of hole taper and circularity in laser percussion drilling. *Int. J. Mach. Tools Manuf.* **42**(9), 985–995 (2002)
39. Shin, J., Mazumder, J.: Shallow angle drilling of inconel 718 using a helical laser drilling technique. *J. Manuf. Sci. Eng.* **139**, 031004–031011 (2017)
40. Sezer, H.K., Li, L., Schmidt, M., Pinkerton, A.J., Anderson, B., Williams, P.: Effect of beam angle on HAZ, recast and oxide layer characteristics in laser drilling of TBC nickel superalloys. *Int. J. Mach. Tools Manuf.* **46**, 1972–1982 (2006)
41. Mullick, S., Agrawal, A., Nath, A.: Effect of laser incidence angle on cut quality of 4 mm thick stainless-steel sheet using fiber laser. *Opt. Laser Technol.* **81**, 168–179 (2016)
42. Schneider, M., Berthe, L., Muller, M., Fabbro, R.: Influence of Incident angle on laser drilling. *ICALEO 2007*, 1205 (2007). <https://doi.org/10.2351/1.5060999>
43. Okasha, M.M., Mativenga, P.T., Li, L., Sezer, H.K.: Laser drilling of nickel alloy: effect of process gases on drilling time and hole quality. *ICALEO 2010*, 127 (2010). <https://doi.org/10.2351/1.5061972>
44. Kamalu, J., Byrdb, P., Pitman, A.: Variable angle laser drilling of thermal barrier coated nimonic. *J. Mater. Process. Technol.* **122**, 355–362 (2002)
45. Leigh, S., Sezer, K., Li, L., Reed, C.G., Cuttell, M.: Statistical analysis of recast formation in laser drilled acute blind holes in CMSX-4 nickel superalloy. *Int. J. Adv. Manuf. Technol.* **43**, 1094–1105 (2009). <https://doi.org/10.1007/s00170-008-1789-6>
46. Marimuthu, S., Antar, M., Dunleavy, J., Hayward, P.: Millisecond fibre laser trepanning drilling of angular holes. *J. Adv. Manuf. Technol. Int.* (2019). <https://doi.org/10.1007/s00170-019-03389-8>
47. Yao, K.C., Lin, J.: The characterization of the hole-contour and plume ejection in the laser drilling with various inclination angles. *Opt. Laser Technol.* **48**, 110–116 (2013). <https://doi.org/10.1016/j.optlastec.2012.10.009>
48. Li, X., Hou, W., Han, B., Xu, L., Li, Z., Nan, P., Ni, X.: Investigation on the continuous wave mode and the ms pulse mode fiber laser drilling mechanisms of the carbon fiber reinforced composite. *Polymers* **12**, 706 (2020). <https://doi.org/10.3390/polym12030706>
49. Grund, D., Orlishausen, M., Taha, I.: Determination of fiber volume fraction of Carbon fiber-reinforced polymer using thermogravimetric methods. *Polym. Test.* (2019). <https://doi.org/10.1016/j.polymertesting.2019.02.031>
50. Heinze, G., Dunkler, D.: Five myths about variable selection. *Transpl. Int.* **30**, 6–10 (2017)
51. Montgomery, D.C.: *Design and Analysis of Experiments*, 10th edn. Wiley, Hoboken (2019)
52. Steen, W.: *Laser Material Processing*. Springer, Berlin (2003)
53. Hejjaji, A., Singh, D., Kubher, S., Kalyanasundaram, D., Gururaja, S.: Machining damage in FRPs: laser versus conventional drilling. *Composites: Part A* (2015). <https://doi.org/10.1016/j.compositesa.2015.11.036>
54. Cheng, C.F., Tsui, Y.C., Clyne, T.W.: Application of a three-dimensional heat flow model to treat laser drilling of carbon fibre composites. *Acta mater.* **46**, 4273–4285 (1998)
55. Ki, H., Pravansu, S., Mohanty, S., Mazumder, J.: Multiple reflection and its influence on keyhole evolution. *J. Laser Appl.* **14**, 1 (2002)
56. Wu, C.W., Wu, X.Q., Huang, C.G.: Ablation behaviors of Carbon reinforced polymer composites by laser of different operation modes. *Opt. Laser Technol.* **73**, 23–38 (2015)
57. Pathak, S.V.: *Enhanced heat transfer in composite materials*. Ohio University (2013)